Letter

Experimental Realization of Multiple Topological Edge States in a One-Dimensional Photonic Lattice

Zhifeng Zhang[1], Mohammad Teimourpour[2], Jake Arkinstall[3], Mingsen Pan[1], Pei Miao[1],

Henning Schomerus[3], Ramy El-Ganainy[2†], and Liang Feng[1,4]*

[, †]Corresponding Author: E-mail: *[*]fenglia@seas.upenn.edu (L.F.); [†]ganainy@mtu.edu (R.E.)

[1]Department of Electrical Engineering, The State University of New York at Buffalo, Buffalo, NY 14260, USA
[2]Department of Physics and Henes Center for Quantum Phenomena, Michigan Technological University, Houghton, MI, 49931, USA
[3]Department of Physics, Lancaster University, Lancaster, LA1 4YB, United Kingdom
[4]Department of Materials Science and Engineering, University of Pennsylvania, Philadelphia, PA 19104, USA

Abstract: Topological photonic systems offer light transport that is robust against defects and disorder, promising a new generation of chip-scale photonic devices and facilitating energy-efficient on-chip information routing and processing. However, present quasi one-dimensional designs, such as the Su-Schrieffer-Heeger (SSH) and Rice-Mele (RM) models, support only a limited number of nontrivial phases due to restrictions on dispersion band engineering. Here, we experimentally demonstrate a flexible topological photonic lattice on a standard silicon photonic platform that realizes multiple topologically nontrivial dispersion bands. By suitably setting the couplings between the one-dimensional waveguides, the lattice can therefore support the transition between multiple different topological phases, and allows the independent realization of the corresponding edge states. Heterodyne measurements clearly reveal the ultrafast transport dynamics of the edge states in different phases at a femto-second scale, validating the designed topological features. Our study equips topological models with enriched edge dynamics and considerably expands the scope to engineer unique topological features into photonic, acoustic and atomic systems.

1. Introduction

The mathematical field of topology, which deals with quantities that preserve their values during continuous deformation, has firmly emerged as a new paradigm for describing new phases of matter since its first applications to condensed matter systems over three decades ago.[1-3] Due to the mathematical equivalence between the paraxial wave equation describing the propagation of light and the Schrödinger equation for the time-evolution of electrons [4], topological concepts seamlessly transfer into the realm of optics and photonics.[5] This realization has inspired a range of versatile topological photonic platforms based on optical resonator arrays,[6-8] waveguide array lattices,[5, 9, 10] photonic crystals,[11-17] and optical quasicrystals.[18, 19] Novel topological features such as symmetry-protected interface states promise a new generation of robust, defect-tolerant and scattering-free photonic circuits[20, 21] with direction-dependent beam dynamics. More recently, a variety of topological lasers have been developed in both one-dimensional [22-24] and two-dimensional configurations[25, 26], which provide robust and highly efficient lasing action.

To date, the SSH Hamiltonian[27] serves as an archetypical model for describing topological physics and designing practical structures. However, the topological features of most conventional models are limited to only two dispersion bands, thereby permitting only a limited range of topological quantum numbers characterizing the bands and gaps, and consequently restricting the accessible nontrivial phases. Much can be gained from richer models with a larger range of nontrivial phases that can be manipulated systematically to realize the formation of independent topological states. While novel topological phases have been observed with time-periodic driving systems,[5] such systems require unique three-dimensional fabrication techniques that are challenging to be applied for on-chip integrated photonics. Here, we successfully demonstrate the formation of topological edge states associated with multiple bandgaps in a discrete photonic lattice based on standard silicon

fabrication techniques. Our system consists of a versatile waveguide array requiring only a small number of fundamental components, and is guided by the concept of generating topological effects through strategic rearrangements that break some crystal symmetries.[28] By varying the design parameters of the waveguides, we observe a topological phase transition from a regime with a single edge state to a regime with two such states at the same edge. These phases are experimentally distinguished by their different localization and diffraction patterns, and further confirmed by their ultrafast transport dynamics at the femtosecond scale. The coexistence of multiple states at a single edge results in intriguing edge dynamics which allows it to be validated by a characteristic spatial beating effect. Based on the powerful universality of topological concepts, these findings can be directly transferred to a wide range of platforms, such as quantum-optical, acoustic, polaritonic and atomic systems.

2. Bowtie Lattice

The conceptual basis of our investigation starts with a two legged ladder system with two sites per unit cell as shown in top panel of **Figure 1(a)**. While such a system possesses two dispersion bands with only a single band gap in between, the associated topological features can be further enriched by taking a nontrivial square root[28] of the orignal system to expand the two dispersion bands into four. This transforms the two bands into four bands arranged symmetrically at positive and negative energies, which become associated with a symmetry-reduced tight-binding system with four sites per unit cell. The latter can be represented as a linear bowtie chain with nearest-neighbor couplings, as shown in the bottom panel of Figure 1a. This bowtie structure can be interpreted as a variant of the ubiquitous Su-Schrieffer-Heeger (SSH)[27] and Rice-Mele (RM)[29] models. To experimentally probe the topological features of the proposed structure, we investigate a photonic implementation

based on an array of coupled waveguides where each waveguide represents a site in the bowtie chain, fabricated on a silicon on insulator (SOI) platform as illustrated in **Figure 1(b)**.

In our waveguide photonic lattice system, the weak coupling results in a discrete diffraction length (the length that light couples completely from one waveguide to the adjacent waveguide) of tens of μm, which is much larger than the operation wavelength of approximately 1550 nm. As a result, the paraxial approximation is valid here[30]. Together with the absence of reflection in the propagation direction and orthogonality of all waveguide modes, the Hamiltonian formalism can be safely applied to our system. In anticipation of our experimental results we use notations from coupled-mode theory, where the propagation constants of the waveguides are denoted by β_n, precisely controlled by designing the dimensions of the cross section of the waveguide, and the coupling of adjacent waveguides is denoted by coefficients κ_n, effectively tuned by the distances between the adjacent waveguides. Each waveguide supports only a single fundamental quasi-TM mode. The loss of the Si waveguides is negligible at the operation wavelength compared to the site energy and coupling strength, so that we can safely assume the propagation constants to be real. The lattice structure can then be viewed as a collection of coupled dimers, where $\tilde{\kappa}$ and κ indicate the coupling between two sites in a dimer and the coupling between dimers, respectively. The dimers are arranged in an alternating fashion in two orientations that we denote as R and L (Figure 1(a)). The lattice chain is designed to be $(RL)_n R$, with (RL) the unit cell. The dynamics of the bowtie chain is then described by the evolution equations

$$i\frac{d\vec{a}_n}{dz} = H\vec{a}_n + T\vec{a}_{n-1} + T^\dagger \vec{a}_{n+1}, \tag{1}$$

where z is the propagation distance along the waveguides and the vectors $\vec{a}_n$ correspond to the field amplitudes of the four waveguides (sites) within the nth unit cell. The coupling of two sites in each dimer is described by the intra-cell matrix H and the adjacent dimers are connected by the inter-cell matrix T. The nonvanishing elements of the intra-unit cell matrix

4

H are given by $H_{11} = H_{44} = \beta_1$, $H_{22} = H_{33} = \beta_2$, $H_{12} = H_{21} = H_{34} = H_{43} = \tilde{\kappa}$, and $H_{23} = H_{32} = \kappa$, while the inter-cell coupling matrix T has only one non-zero entry $T_{14} = \kappa$. Without any loss of generality, we assume that $\beta_1 > \beta_2$ and take all the coupling coefficients to be real.

The topological bowtie lattice provides control to design different Bloch eigenstates formed through hybridization of the supermodes associated with the dimers/waveguides. As shown in Figure 1(b), for a nonvanishing detuning $\Delta\beta$ of the propagation constants between the large and small waveguide in each of the dimer, the supermodes are highly localized in the large (base) or small (vertex) waveguides. Two supermodes each are close to resonance, experiencing effective coupling strengths alternating between strong and weak. This effect can be viewed as two SSH Hamiltonians (SSH $_I$ and SSH $_{II}$) occupying the same space yet having independent topological quantum numbers as shown in the lower panel of Figure 1(b). As each SSH model creates two eigenvalues $\lambda_\pm$, the designed bowtie lattice is expected to demonstrate four dispersion bands, which is indeed borne out by direct modelling (**Figure 1(c)**). The coupling strengths and propogation constants are engineered to demonstrate different topological phases and thus realize the related edge states. In the top panel of Figure 1c, the design parameters were chosen to be $\tilde{\kappa} = 0.127 \; \mu m^{-1}$, $\kappa = 0.5\tilde{\kappa}$ and $\beta_1 = -\beta_2 = \tilde{\kappa}$. As expected from the previous discussion, the system resembles two separate SSH Hamiltonians giving rise to two upper (SSH $_I$) and two lower (SSH $_{II}$) bands. The two isolated eigenvalues in the spectrum (one in the upper and another in the lower band gaps) correspond to states localized at the left and right edge. This is in contrast to the conventional SSH model, for which the two edge states would lie in the same gap. The middle and lower panels of Figure 1(c) highlight a crucial additional feature of this model—the existence of a third, central gap that separates the two effective SSH models. The design parameters are the same as used in the top panel, but for $\kappa = \sqrt{2}\tilde{\kappa}$ and $2\tilde{\kappa}$, respectively. The central gap closes at $\kappa = \sqrt{2}\tilde{\kappa}$ while in the lower panel the gap is again opened. This band inversion gives rise to

an additional pair of isolated eigenvalues, which are accompanied by the emergence of two new edge states. These edge states are associated with the spectral symmetry of the bowtie chain, which induces an additional topological quantum number. In an infinite long chain, the two low-energy solutions near $k = 0$ give rise to two slowly varying fields that can be grouped into a spinor φ. Its evolution takes the form of a Jackiw-Rebbi model $id\varphi/dz = H_{eff}\varphi$ with an effective Hamiltonian $H_{eff} = m\sigma_z + v_F\sigma_y\hat{p}_x$,[33] again in complete analogy with the SSH model.[34] All three effective models are therefore associated with a chiral symmetry $\sigma_x H_{eff}\sigma_x = -H_{eff}$ guaranteeing topological physics in each gap.

The detailed edge features of the complete system can be understood by inspecting the Zak phase[31] and Witten index[32] associated with each bulk band and each bandgap, respectively. The Witten index is related to the reflection phase at a spectral symmetry point and can be calculated form the associated Zak phase of the bulk bands, which determine the reflection phases at the band edges. A detailed calculation for our setup [28] results in the relations $W_1 = -(Z_1 - Z_4)$ for the upper band gap, $W_2 = (Z_2 - Z_3)$ for the lower band gap, and $W = -(Z_2 + Z_3)$ for the central band gap, where Z_i are the Zak indices ordered from the top to the bottom band, as listed in **Table 1.** With the designed termination of the unit cell, we expect to find edge states in each gap when the corresponding Witten index takes the value -1, corresponding to fulfillment of the effective hard-wall boundary conditions. For the experiment, we exploit that the Witten index W determining the existence of a topological edge state in the central bandgap can be controlled by solely tuning the intra-dimer coupling.

3. Experimental implementation
3.1 Design and fabrication

A straightforward way to demonstrate the topological features is to excite the system at its edge. In our photonic lattice design, the initial state is set up as the mode of the outmost

waveguide where its propagation constant is fixed. By coupling light to one edge of the topological photonic lattice, all existing edge states at that edge will be excited because of the large overlap with the input state. We aim to identify the different topological phases through the discrete diffraction, localization and interference signatures of light transport. This is greatly facilitated when the light transport dynamics becomes directly visualized over the whole propagation distance, revealing the evolution of the transverse light distribution for a propagation distance z. To measure the light transport in the far field, we intentionally introduced periodic hole patterns on top of the waveguide lattice, satisfying a phase matching condition to coincide with the effective wavelength of the guided mode propagating inside of the waveguides and to efficiently couple the well-confined guided light into the upward direction, as illustrated in **Figure 2(a)**. For the experiments, we fabricated three different samples of the photonic lattice with controlled physical parameters corresponding to different configurations I, II and III as defined in **Table 2.** On an SOI platform, the samples were patterned using electron beam lithography, followed by reactive ion etching to form the bowtie waveguides lattice with the hole patterns. The diameter of each hole was chosen to be 150 nm, which provided a good balance between the upward coupling efficiency and the insertion loss. The SiO_2 cladding layer was subsequently deposited using plasma enhanced chemical vapor deposition (PECVD), which ensures symmetric confinement of the light field inside the waveguides and increases the efficiency of upward coupling. Each sample consisted of 18 guiding channels. The scanning electron microscope pictures before deposition of the SiO_2 cladding are shown in **Figure 2(b)**.

3.2 Results

The effective realization of the edge states in different topological phases was both experimentally and numerically validated through the imaging of the light transport at the sample plane in three different configurations. A tunable continuous-wave fiber laser

(adjusted to operate at the free space wavelength of 1555 nm) was directly connected to a polarization-maintaining tapered fiber that efficiently delivered a TM polarized laser beam into the right-most edge waveguide of the on-chip bowtie waveguides lattice to carry out the averaged power measurement. Figure 3(a) corresponds to configuration I ($\kappa = 0.5\tilde{\kappa} = 0.064\mu m^{-1}$), where our theoretical model predicts a single edge state confined in the bottom waveguide, originating from the Witten index $W_1 = -1$ for the upper finite-energy bandgap; this ensures a single topological edge state in that gap. Meanwhile, the Witten indices in the central and lower bandgaps are designed to be $W = W_2 = 1$, leading to no topological edge state in these gaps. The optical intensity remains well confined to the launching channel (i.e. the bottom waveguide), while close inspection shows the absence of any appreciable intensity fluctuations. For configuration II ($\kappa = \sqrt{2}\tilde{\kappa} = 0.180\mu m^{-1}$) (Figure 3(b)), light localization at the edge persists as the Witten index for the finite energy gaps remains the same as that in configuration I. However, a clear signature of discrete diffraction across all the waveguides in the transverse direction is also observed, conforming with the general expectations for the closure of the central bandgap, which results in a nearly linear band-dispersion [30] that facilitates the observed secondary emission. From our modelling, the overlap between the input states and the bulk states becomes maximal at this point in Figure 3(d). Increasing the coupling κ to the value in configuration III ($\kappa = 2\tilde{\kappa} = 0.255\mu m^{-1}$) leads to a reopening and inversion of the central bandgap. The Witten index of the central bandgap switches from $+1$ to -1, and fulfills the boundary condition [28] to form an edge state also inside of this bandgap. Since the Witten indices W_1 and W_2 for the finite energy bandgaps remain unchanged, the system now support two edge states located in different bandgaps, and the distinct propagation constants of these two states leads to interference beating along the launch waveguide (Figure 3(c)). Since the reopened central bandgap is not as wide as that in

8

configuration I, the corresponding edge state resides close to the band edge, such that there also exists pronounced diffraction into the bulk.

In the experiment some small intensity fluctuations are also observed in configurations I and II (but much smaller if compared with case III). This is due to the small overlaps between the input state and the extended bulk states (Figure. 3(d)) as well as some disorder (see supporting information for details). Some of these fluctuations result from the resolution of approximately 1 μm in our far-field imaging system, which thereby also captures light from the adjacent waveguides. To address this issue, we applied the time-resolved spatial-heterodyne imaging technique [35], which provides the spatial distribution of the EM amplitude versus time. Thus, we could characterize the ultrafast transport dynamics in the observed edge states. Instead of the CW laser, we used a femto-second pulsed laser source with pulse width of 160fs centered at 1550nm. A modified Mach-Zehnder interferometer with a variable delay line was built to perform the ultra-fast time resolved test. Consistent with the average power measurements, the temporal evolution of the wave packet in the bowtie lattice further confirms the topological transition among the three designed configurations (Fig. 4). For configuration I, the launched wave packet couples mainly into a single edge state. Since the edge state is localized within the wide central bandgap, the pulse propagation is robust against variations of the neighboring couplings and thus remains confined in the right-most waveguide (see **Movie S1** in Supporting Information). The intensity variations in the neighboring waveguides can be understood to result from the mismatch between the excitation in a single waveguide and the actual modal profile of the edge state, which extends over a few waveguides. These ultrafast temporal measurements provide access to quantitative characteristics of the edge state [36].

All the edge states are associated with distinct dynamical properties encoded in the effective group and phase index, which provide additional quantitative assessments of each

state. In configuration I, the group index $n_g = 3.30 \pm 0.012$ (calculation details can be found in supporting information) can be retrieved through pulse positions traveled at different time delays, corresponding to an effective index of $n_{eff} = 1.67 \pm 0.012$ that agrees well with the simulation $n_{eff} = 1.72$. For configuration II, it is clearly demonstrated that the dynamical transport of the single edge state is accompanied by a secondary emission, revealing the closure of the central bandgap. Their interference, while weak, slightly distorts the field distribution and the propagation of the wave packet in the launching channel (see **Movie S2** in Supporting Information). The measured group index is consistently lower, $n_g = 3.23 \pm 0.011$ with $n_{eff} = 1.66 \pm 0.011$. For configuration III, the dynamical evolution of the wave packet is revealed by the interference beating [37-39] due to the co-propagation of two edge states with distinct propagation constants (see also **Movie S3** in Supporting Information). The measured group index $n_g = 3.18 \pm 0.015$ in this case is the averaged group index of the two edge states. Their respective effective indices are $n_{eff,1} = 1.70 \pm 0.015$ and $n_{eff,2} = 1.65 \pm 0.015$. In contrast, a uniformly arranged trivial waveguide array shows a diffraction pattern corresponding to free spreading and reflection of the wave across the whole array. This is distinct from the topological edge modes observed in the previous 3 configurations. (See **Movie S4** in the Supporting Information.)

While the samples are designed for excitation at the outmost waveguide, observation of the diffraction from the edge to the bulk state also provides convincing evidences to judge if a band gap is closed or open. Meanwhile, the appearance of the beating patterns directly reveals the engagement of a second edge mode, which arises in the newly opened second topological bandgap. This configuration with multiple topological bandgaps is in contrast with recent work where two topological edge states emerge through band folding in the same bandgap.[40] In our case, both the time-averaged and the temporally resolved experimental

results confirm that the multiple quantum numbers of out photonic lattice offer more flexible control over the topological states.

4. Conclusion

In summary, by considering the non-trivial square root of a two legged ladder system, we designed and experimentally demonstrated a versatile photonic lattice with multi-band topology. Compared with the conventional Su-Schrieffer Heeger and Rice-Mele models, the lattice offers additional spectral symmetries that enrich the topological features and enable to induce independently tuned edge states. We experimentally investigated the ultrafast beam transport dynamics to validate the supported topological characteristics. Through systematically manipulating the couplings in the lattice, the topological nature of multiple dispersion bands can be effectively engineered with a desired Witten index in different energy bandgaps, enabling the versatile realization of topologically-induced edge state dynamics.

Supporting Information
Additional supporting information may be found in the online version of this article at the publisher's website.

Movie S1
Movie S2
Movie S3
Movie S4

References

[1] R. B. Laughlin, *Phys. Rev. B* **23**, 5632 (1981).

[2] D. J. Thouless, M. Kohmoto, M. P. Nightingale, M. Den Nijs, *Phys. Rev. Lett.* **49**, 405 (1982).

[3] F. D. M. Haldane, *Phys. Rev. Lett.* **61**, 2015 (1988).

[4] D. N. Christodoulides, R. I. Joseph, *Optics Lett.* **13**, 794-796(1988).

[5] M.C. Rechtsman, J.M. Zeuner, Y. Plotnik, Y. Lumer, D. Podolsky, F. Dreisow, S. Nolte, M. Segev, A. Szameit, *Nature* **496**, 196-200 (2013).

[6] M. Hafezi, E. A. Demler, M. D. Lukin, J. M. Taylor, *Nat. Phys.* **7**, 907-912 (2011).

[7] M. Hafezi, S. Mittal, J. Fan, A. Migdall, J. M. Taylor, *Nat. Photon.* **7**, 1001-1005 (2013).

[8] G. Q. Liang, Y. D. Chong, Phys. *Rev. Lett.* **110**, 203904 (2013).

[9] M.C. Rechtsman, Y. Plotnik, J.M. Zeuner, D. Song, Z. Chen, A. Szameit, M. Segev, Phys. *Rev. Lett.* **111**, 103901 (2013).

[10]S. Weimann, M. Kremer, Y. Plotnik, Y. Lumer, S. Nolte, K.G. Makris, M. Segev, M.C. Rechtsman, A. Szameit, *Nat. Mater.* **16**, 433-438 (2017).

[11]Z. Wang, Y. D. Chong, J. D. Joannopoulos, M. Soljačić, *Nature* **461**, 772-775 (2009).

[12]A. B. Khanikaev, S. H. Mousavi, W. Tse, M. Kargarian, A. H. MacDonald, G. Shvets, *Nat. Mater.* **12**, 233-239 (2013).

[13]L. H. Wu, X. Hu, *Phys. Rev. Lett.* **114**, 223901 (2015).

[14]C. He, X. C. Sun, X. P. Liu, M. H. Lu, Y. Chen, L. Feng, Y. F. Chen, *PNAS* 113, 4924-4928 (2016).

[15]B. Zhen, C. W. Hsu, L. Lu, A. D. Stone, M. Soljačić, *Phys. Rev. Lett.* **113**, 257401 (2014).

[16]S. A. Skirlo, L. Lu, Y. Igarashi, Q. Yan, J. Joannopoulos, and M. Soljačić, *Phys. Rev.*

Lett. **115**, 253901 (2015).

[17] A. Kodigala, T. Lepetit, Q. Gu, B. Bahari, Y. Fainman, B. Kanté, *Nature* **541**, 196-199 (2017).

[18] M. Verbin, O. Zilberberg, Y. E. Kraus, Y. Lahini, Y. Silberberg, *Phys. Rev. Lett.* **110**, 076403 (2013).

[19] M. A. Bandres, M. C. Rechtsman, M. Segev, *Phys. Rev. X* **6**, 011016 (2016).

[20] H. Schomerus, *Opt. Lett.* **38**, 1912-1914 (2013).

[21] C. Poli, M. Bellec, U. Kuhl, F. Mortessagne, H. Schomerus, *Nat. Commun.* **6**, 6710 (2015).

[22] H. Zhao, P. Miao, M. H. Teimourpour, S. Malzard, R. El-Ganainy, H. Schomerus, L. Feng, *Nat. Commun.* **9**, 981 (2018).

[23] M. Parto, S. Wittek, H. Hodaei, G. Harari, M. A. Bandres, J. Ren, M. C. Rechtsman, M. Segev, D. N. Christodoulides, M. Khajavikhan, *Phys. Rev. Lett.*, **120**, 113901 (2018).

[24] P. St-Jean, V. Goblot, E. Galopin, A. Lemaître, T. Ozawa, L. Le Gratiet, I. Sagnes, J. Bloch, A. Amo, *Nat. Photon.* **11**, 651 (2017).

[25] G. Harari, M. A. Bandres, Y. Lumer, M. C. Rechtsman, Y. D. Chong, M. Khajavikhan, D. N. Christodoulides, M. Segev, *Science* 359, 6381 (2018).

[26] M. A. Bandres, S. Wittek, G. Harari, M. Parto, J. Ren, M. Segev, D. N. Christodoulides, M. Khajavikhan, *Science* 359, 6381 (2018)

[27] W. Su, J. R. Schrieffer, A. J. Heeger, *Phys. Rev. Lett.* **42**, 1698 (1979).

[28] J. Arkinstall, M. H. Teimourpour, L. Feng, R. El-Ganainy, H. Schomerus, *Phys. Rev. B* **95**, 165109 (2017).

[29] M. J. Rice, E. J. Mele, *Phys. Rev. Lett.* **49**, 1455 (1982).

[30] D. N. Christodoulides, F. Lederer, Y. Silberberg, *Nature* **424**, 817 (2003).

[31] J. Zak, *Phys. Rev. Lett.* **62**, 2747 (1989).

[32] E. Witten, *Nucl. Phys. B* **202**, 253-316 (1982).

[33] R. Jackiw, C. Rebbi, *Phys. Rev. D* **13**, 3398 (1976).

[34] S. Ryu, Y. Hatsugai, *Phys. Rev. Lett.* **89**, 077002 (2002).

[35] R. Rokitski, K. A. Tetz, Y. Fainman, *Phys. Rev. Lett.* **95**, 177401 (2005).

[36] M. Abashin, K. Ikeda, R. Saperstein, Y. Fainman, *Opt. Lett.* **34**, 1327-1329 (2009).

[37] R. Rokitski, P. C. Sun, Y. Fainman, *Opt. Lett.* **26**, 1125-1127 (2001).

[38] L. Feng, M. Ayache, J. Huang, Y.L. Xu, M.H. Lu, Y.F. Chen, Y. Fainman, A. Scherer, *Science* **333**, 729-733 (2011).

[39] A. Regensburger, M.A. Miri, C. Bersch, J. Näger, Onishchukov, G. D.N. Christodoulides, U. Peschel, *Phys. Rev. Lett.* **110**, 223902 (2013).

[40] S. Yves, R. Fleury, T. Berthelot, M. Fink, F. Lemoult, G. Lerosey, *Nat. Commun.* **8**, 16023 (2017).
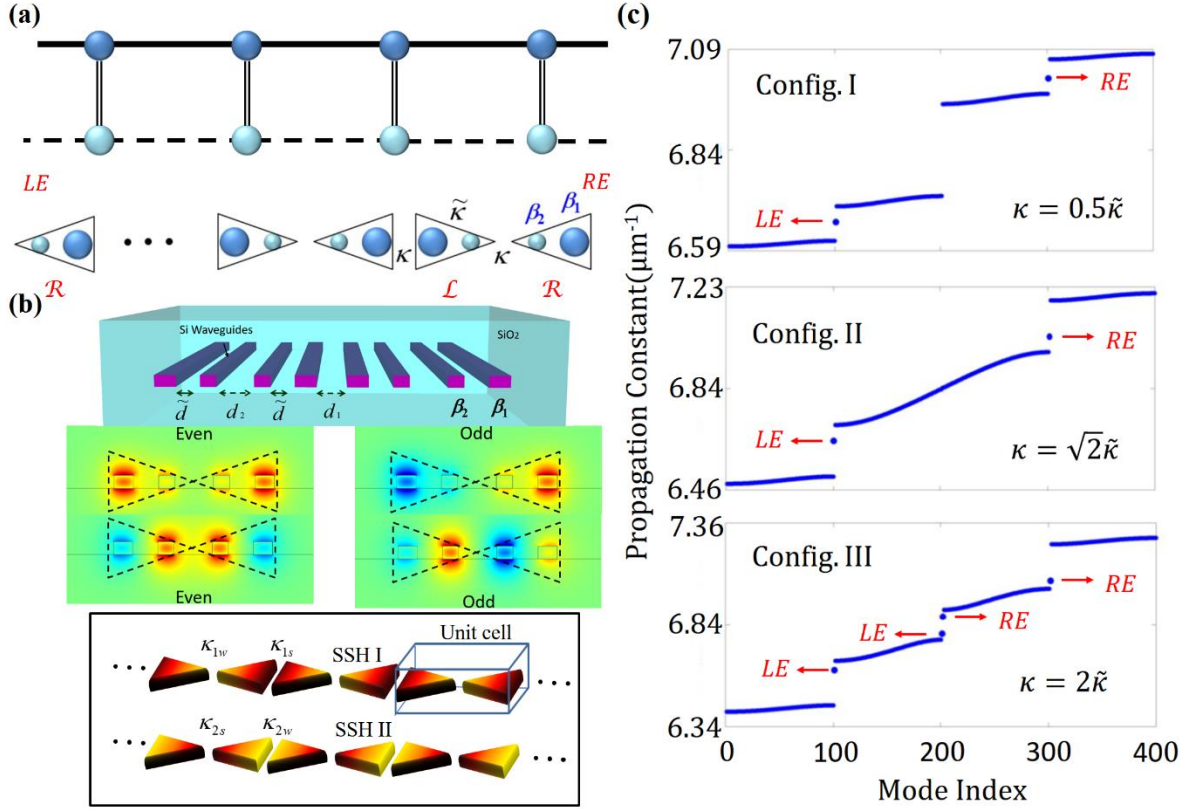
Figure 1. Bowtie topological lattice. (a) Two-legged ladder model having identical sites (top panel). Single and double lines represent couplings of different strength; the dashed lines signify couplings of opposite sign from the solid lines. Taking the square root and a Z_2 gauge transformation of this model results in the bowtie chain shown in the lower panel, with alternating couplings κ, $\tilde{\kappa}$ and staggered sequence of onsite energies $\beta_1, \beta_2, \beta_2, \beta_1, \dots$. As indicated, this can be interpreted as a sequence of oppositely orientated dimers, labelled by L and R. The left edge of the chain is marker as LE and the right edge is marked as RE. (b) Implementation of the bowtie lattice using silicon waveguides embedded in silica cladding, where fundamental TM_{00} mode hybridizations are formed for an isolated unit cell. The waveguide array consists of two different types of waveguides, having the same height $h = 230$nm but different widths: $w_1 = 300$nm and $w_2 = 350$nm, corresponding to propagation constants $\beta_1 = 6.713\mu m^{-1}$ and $\beta_2 = 6.968\mu m^{-1}$, respectively. These parameters translate into an onsite detuning of $\Delta\beta = 0.255\mu m^{-1}$. In our design, different waveguides are arranged

15

in pairs with having β_1 and β_2, with a fixed separation $\tilde{d} = 475$nm that corresponds to an intra-dimer coupling $\tilde{\kappa} = 0.127\mu m^{-1}$. The inter-dimer distances between the two types of waveguide are denoted by $d_{1,2}$, and are tuned to yield an identical coupling of κ. Lower panel shows the formation of two independent SSH Hamiltonians as a result of the eigenstate hybridization between the local modes of the R and L dimers. In SSH$_I$, the states are more localized at the bases giving rise to alternating strong and weak coupling at the bases/vertices respectively, and the converse for SSH$_{II}$. (c) Band structures of bowtie arrays of the form $(RL)_{100}R$ with the designed parameters. For $\kappa = 0.5\tilde{\kappa}$ (top pannel), the upper and lower bandgaps each support a single defect edge state, one on each edge. As the coupling reaches $\kappa = \sqrt{2}\tilde{\kappa}$ (middle panel), the two inner bands merge, closing the central bandgap. Further increasing the coupling to $\kappa = 2\tilde{\kappa}$ (bottom panel) the central gap is open again, which results in the emergence of two new edge states associated with an effective SSH model for the central gap. Edge states are marked with LE or RE to indicate their residence edge.
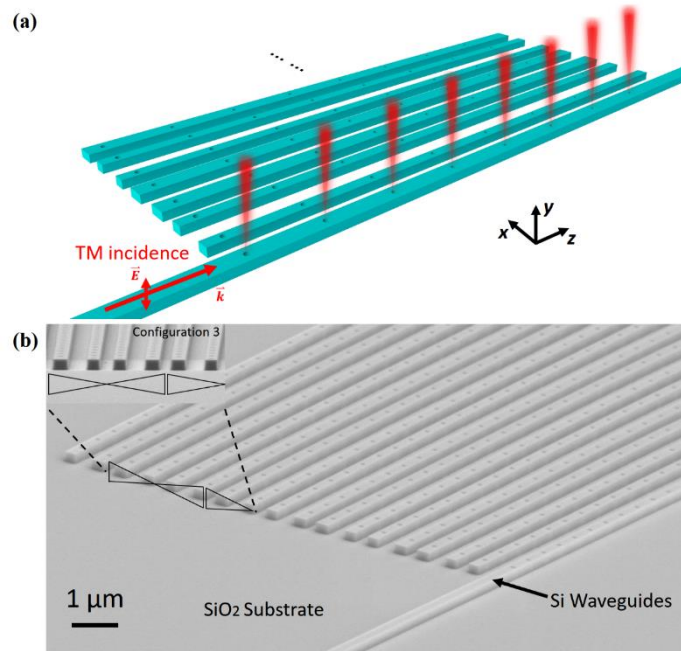
Figure 2. Experimental implementation of bowtie topological photonic lattices. (a) Configuration of the bowtie waveguide array with periodic hole patterns on an SOI platform, designed to measure the beam propagation dynamics across the length of the device. The on-top holes with a diameter of 150 nm are designed to couple light out of the waveguides, which extract light to free space to reveal the propagation of the light inside the structure in far field. (b) Scanning electron microscope pictures of the device (configuration III) before deposition of the SiO$_2$ cladding. The fabricated device consists of 18 waveguides. The periodicity of the holes is matched to the effective wavelength of the quasi-TM mode inside the waveguides (934 nm for the base waveguides and 901 nm for the vertex waveguides), which results in vertical light extraction. Inset zoom in the picture shows the cross section of the bowtie waveguides structure in configuration III.
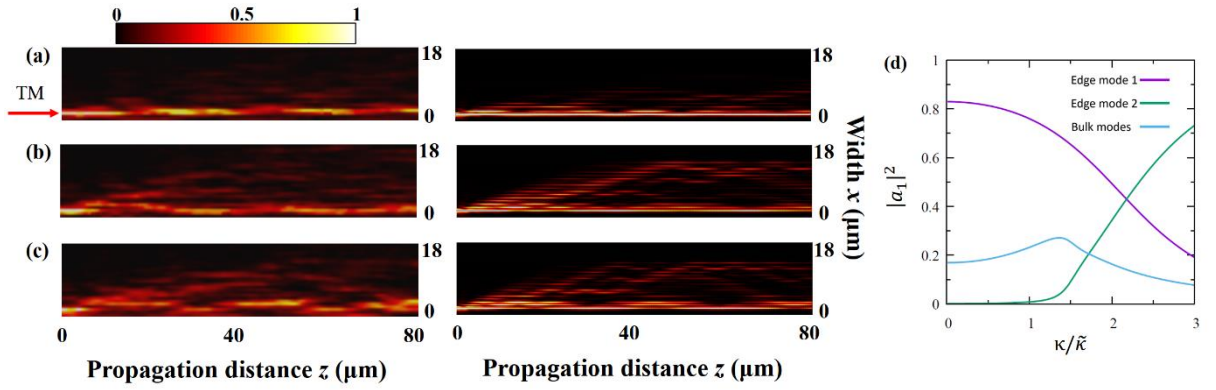
Figure 3. Experimental and EM simulation beam transport in the bowtie topological waveguide lattices and modal overlap of initial state (delta excitation at the bottom waveguide) with the different supermodes of the system (edge-defect and bulk states). (a)-(c) Light field intensity images under TM polarized continuous wave incidence at a wavelength of 1555 nm for configurations I, II and III (top to bottom panels), clearly demonstrating the transition between different topological phases. Due to the insertion loss arising from the hole array, the total propagating power across the bowtie waveguides lattice slightly decreases as a function of the propagation distance. Normalizing the recorded images with respect to the total power across every propagation cross section, so that the total power at any distance z remains a constant, enables a fair comparison between the experimental results (left panels) and simulations (right panels). (d) Predicted modal overlap of the initial input state with the edge states and the bulk states for the 18 waveguides experimental system, as a function of the hopping amplitude. $|a_1|^2$ describes the modal overlaps between the input and excited states. The modal overlap between the input mode and the bulk mode, while weak compared to the overlap with edge states, leads to discrete diffraction into bulk and small intensity fluctuations observed in (a)-(c). Note that the same set of samples are used as for Figure 4. Images are zoomed in to show the details.
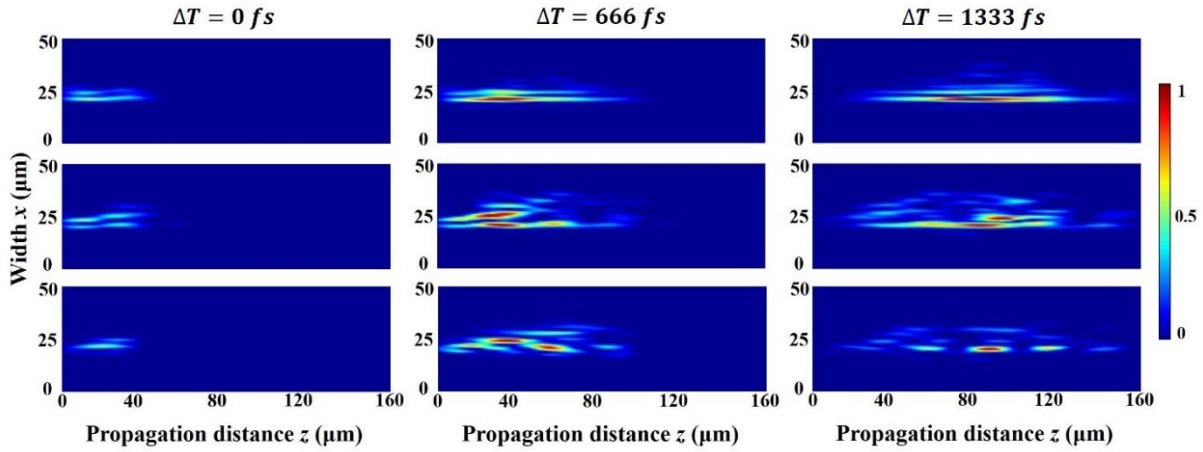
Figure 4. Measured ultrafast transport dynamics in the bowtie topological waveguide lattices. Temporal evolution of spatial intensity of the wave packet is captured with a time delay of ~66.6 fs for configurations I, II and III (top, middle, and bottom panels, respectively). Images are normalized with the same input power, assuming a lossless propagation in the z direction. Field intensity spatial maps in left, middle, and right colums correspond to different time delays at $\Delta T = 0, 666,$ and 1333 fs, respectively, showing the wave packet entering the lattice, the formation of the edge states at the beginning of the lattice, and the transport of the edge states in the lattice. More detailed information can be found in Movies S1, S2, and S3 in Supporting Information.

Table 1. Zak phase and Witten index of 3 configurations in different topological phases.

Band/Gap	Upper Band 1 Z_1	Upper Gap W_1	Upper Band 2 Z_2	Central Gap W	Lower Band 1 Z_3	Lower Gap W_2	Lower Band 2 Z_4
Config.I	$Z_1 = 0$	$W_1 = -1$	$Z_2 = 0$	W=1	$Z_3 = -1$	$W_2 = 1$	$Z_4 = -1$
Config.II	$Z_1 = 0$	$W_1 = -1$	$Z_2 = 0$	N.A.	$Z_3 = -1$	$W_2 = 1$	$Z_4 = -1$
Config.III	$Z_1 = 0$	$W_1 = -1$	$Z_2 = 1$	W=-1	$Z_3 = 0$	$W_2 = 1$	$Z_4 = -1$

Table 2. Design parameters of 3 configurations in different topological phases.

Edge to edge separation	Configuration I $\kappa = 0.5\tilde{\kappa} = 0.064\mu m^{-1}$	Configuration II $\kappa = \sqrt{2}\tilde{\kappa} = 0.180\mu m^{-1}$	Configuration III $\kappa = 2.0\tilde{\kappa} = 0.255\mu m^{-1}$
d_1	700nm	430nm	345nm
d_2	610nm	365nm	290nm

Graphical Abstract